The final publication is available at

http://doi.org/10.1002/celc.201800435

Additional Information

Electrochemical dating of archaeological gold

Antonio Doménech-Carbó*[a], Fritz Scholz[b], María Teresa Doménech-Carbó[c], Joan Piquero-Cilla[a], Noemí Montoya[a], Trinidad Pasíes-Oviedo[d], Manuel Gozalbes[d], José Manuel Melchor-Montserrat[e], Arturo Oliver[f]

[a] *Department of Analytical Chemistry, University of Valencia, Dr. Moliner, 50, 46100 Burjassot (Valencia) Spain*
[b] *Universität Greifswald, Institut für Biochemie, Felix-Hausdorff Straße 4, 17487, Greifswald, Germany.*
[c] *Institut de Restauració del Patrimoni, Universitat Politècnica de València, Camí de Vera 14, 46022, València Spain.*
[d] *Museu de Prehistòria de València. Corona 36, 46003, Valencia, Spain.*
[e] *Museu Arqueològic Municipal de Borriana, Plaça de la Mercé, s/n | 12530 Borriana (Castelló).*
[f] *Museu de Belles Arts de Castelló, Avenida Hermanos Bou, 28. 12003. Castellón de la Plana.*

* Corresponding author, e-mail: antonio.domenech@uv.es.

Abstract

For the first time a dating method for archaeological gold objects is described which is based on a corrosion clock and electrochemical measurements. The method has been calibrated with the help of a series of well-documented gold specimens from different prehistory museums covering the last 2600 years.

Keywords: Archaeology; Dating; Gold; Electrochemistry.

Dating (age determination) is a fundamental analytical demand in archaeology and history of art. This analytical goal is particularly difficult for metal objects, which, in principle, can only be indirectly dated by means of the well-established radiocarbon (1) and aminoacid racemization (2) methods when traces of organic matter accompany the metal object, or –also indirectly– by analyzing the alloy composition (including isotope patterns) and comparing the latter with that of known samples. For 'direct' dating of metal, only few approaches have been recently reported, namely, lead dating based on measurements of superconducting Meisner effect (3) and gold dating based on He, U, and Th analysis (4).

In this context, we previously described the application of electrochemical measurements for dating lead (5) and copper/bronze (6) objects using the voltammetry of immobilized particles (VIMP) methodology. This is a solid-state electrochemical technique which permitting to use only a few nanograms of sample which are abrasively transferred from the corrosion layers of the object to the surface of a graphite electrode. As all other dating methods, which rely on chemical reactions, the above suffer from variable environmental conditions during corrosion and the variability of the metal composition and metallographic structures so that their application is limited to case studies where the chemical conditions kept rather constant over the entire time span to be dated.

Application of chemical methods for dating gold was of archaeological interest because of its use since the antiquity for jewelry, cult figures, coinage, prestige items, etc. and its high chemical stability. This last property makes gold particularly interesting for defining an archaeological clock because, in contrast to copper, lead, etc., metals which undergo more or less intense corrosion, the alteration of gold surfaces is minimal and less influenced by the local conditions of preservation, which challenges the detection and monitoring of gold aging. This process, which is also causing the loss of surface brightness, has been attributed to physical adsorption of oxygen and water and formation of oxides of impurities (7), a rather complex scenario on the gold surfaces. Recent studies using Raman spectroscopy have shown the presence of $\cdot O$ radicals adsorbed on Au(111) and Au(211) faces, as well as $\cdot OH$, $\cdot OOH$, and O_2.adsorbates and even $Au(OH)_3$ and Au_2O_3 species (8,9) (see Supplementary information). Reinforcing

such studies, it has been reported that the attack of chemically generated $\cdot$OH radicals via Fenton reaction produced significant morphological changes in gold surfaces (10) and smoothing asperities (11).

Electrochemical studies confirmed this complex scenario. Thus, in contact with aqueous H_2SO_4 solutions, gold is electrochemically oxidized at potentials around 1.1 V vs. Ag/AgCl via the initial adsorption of $\cdot$OH on the metal surface, rapidly followed by oxidation including place exchanges between gold and oxygen atoms, leading to a quasi three-dimensional oxihydrate layer (12), which can be further dehydrated, while in contact with HCl media, oxidative dissolution to form Au(III) complexes occurs. Interestingly, the voltammetric signals for 'bulk' gold are accompanied by minor, secondary signals which can be attributed to the oxidation of active gold sites (13), gold atoms coordinatively unsaturated or occupying defect lattice sites, formed as a result of place-exchange processes in which oxygen surface atoms penetrate deeper layers, a situation ultimately related to spillover features in metal oxide/metal catalysts (14).

The existence of this rich oxidative electrochemistry and its sensitivity to minute changes in the properties of the metal surface, suggested the possibility of an electrochemical monitoring of gold aging. Our voltammetric data for polycrystalline gold electrodes and nanosamples from gold artifacts attached to graphite bars in contact with aqueous HCl and H_2SO_4 solutions produced well-defined anodic signals (see Figure 1a) for the oxidation of bulk gold (A_{Au}) and active sites (A_*), this second being reinforced in the 2nd scan.

The VIMP methodology was applied to a set of archaeological coins and jewelry provided by the Museums of Prehistory of Valencia, Borriana and Castelló (Spain) covering a time interval from the 4th century BCE to nowadays, all containing percentages of Au of 90 ± 5 wt-% accompanied by Ag (5-10 wt-%) and Cu (1-5 wt-%) (see Supplementary information, Table S.1). Voltammetric data denoted a growth of the $A_{Au}(*)$ signals relative to A_{Au} with age, a feature previously observed for natural gold samples (15).

This feature was found to be consistent with accelerated electrochemical aging of gold surfaces by means of the application of successive oxidative and reductive potentials as illustrated in Figures 1b-d, corresponding to AFM topographic images of a microcrystalline gold plate in contact with 0.10 M H_2SO_4 aqueous solution. After applying an oxidative potential at A_{Au}, the gold surface, which originally exhibited a relatively uniform roughness (Fig. 1b), became slightly rougher and covered by rounded features alternating with several gross features (Fig. 1c) attributable to local formations of gross oxide humps. The subsequent application of a reductive potential to this oxidized surface regenerates a gold surface whose roughness differs from the parent surface, also incorporating peaked features and retaining a few gross humps (Fig. 1d). These observations are consistent with an increase of coordinatively unsaturated gold sites with age.

Figure 2 shows the calibration graph obtained upon application of a sequence of two positive-going potentials using 0.10 M HCl as the electrolyte (see Supplementary materials for a detailed description) using the aforementioned set of archaeological samples, expressed as the time variation of the ratio of the peak currents of the above signals, respectively in the 2nd and 1st scans, $i(A_*(2))/i(A_{Au}(1))$. After testing different models for adsorption kinetics, the most satisfactory fit was obtained for Lagergren's equation (16), corresponding to a pseudo-first order rate law, represented as a continuous line in Figure 2, following the equation $i(A_*(2))/i(A_{Au}(1)) = H - Qe^{-kt}$, taking $H = 0.71\pm0.05$, $Q = 0.58\pm0.08$, and $k = (5.8\pm0.4) \times 10^{-4}$ years^{-1} which. Analysis of errors (see Supplementary information) based on this equation yields a time-dependent uncertainty increasing with age. The dispersion of data points was relatively low and resulted probably from the uniformity of the composition of the studied objects, all with wt. percentages of gold around 90% .

The proposed electrochemical method for dating gold objects is the first which is based on a real clock, here the corrosion process. At the expense of refinements and testing a more extensive set of samples, it is most remarkable that the results prove this clock to be going on a constant pace, and practically independent of the corrosion environment, involving an essentially non-invasive sampling, limited to a few nanograms of the artifacts surface. The low uncertainty of age determination (e.g., ±180 years at ages of

ca. 2000 years) (see Supplementary information, Annex A.2 for calculation of the uncertainty in age determination) makes it most attractive for application in archeometry.

Author contributions: A.D.-C. designed the research and wrote the manuscript, F.S. discussed the results with A,D.-C and revised the manuscript, M.T.D.-C. performed AFM-VIMP experiments, N.M. performed Raman and SEM/EDX experiments, J.P.-C. performed voltammetric measurements, T.P.-O., M.G., J.M.M.-M. and A.O. provided the archaeological identification and characterization of gold objects.

References

1. M. Balter, *Science*, **313**, 1560 (2006).

2. H.N. Poinar et el., *Science* **272**, 864 (1996).

3. S. Reich, G. Leitus, S. Shalev, *New J. Phys*. **5**, 99.1 (2003).

4. O. Eugster et al. *Archaeometry* **51**, 672 (2009).

5. A. Doménech-Carbó, M.T. Doménech-Carbó, M.A. Peiró-Ronda, *Anal. Chem.* **83**, 5639 (2011).

6. A. Doménech-Carbó et al. *Angew. Chem. Int. Ed*. **53**, 9262 (2014).

7. R.C. Plumb, N. Thakkar, N. *J. Phys. Chem*. **69**, 439 (1965).

8. J. Desilvestro, M.J. Weaver, *J. Electroanal. Chem*. **209**, 377 (1986).

9. B.S. Yeo et al. *ChemPhysChem* **11**, 1854 (2010).

10. F. Scholz, et al., *Angew. Chem. Int. Ed*. **46**, 8079 (2007).

11. A. Nowicka, et al., *Angew. Chem. Int. Ed*. **49**, 3006 (2010).

12. R.L. Doyle, M.E.G. Lyons, *J. Solid State Electrochem*. **18**, 3271 (2014).

13. L.D. Burke, A.P. O'Mullane, *J. Solid State Electrochem*. **4**, 285 (2000).

14. J.M. Jaksic, et al., *J. Phys. Chem. C* **114**, 18298 (2010).

15. A. Doménech-Carbó, et al., *Electrochem. Commun.* **85**, 23 (2017).

16. W. Plazinski, W. Rudzinski, *J. Phys. Chem. C* **113**, 12495–12501 (2009).

Figures

Figure 1. a) First (black) and second (red) positive-going linear potential scan voltammograms recorded for a microcrystalline gold sample attached to graphite bar in contact with air-saturated 0.10 M H_2SO_4 aqueous solution. Potential scan rate 50 mV s^{-1}. b-d) AFM topographic images (1x1x0.01 μm) of a gold plate in contact with 0.10 M H_2SO_4 aqueous solution b) before and c) after application of a potential of +1.25 V for 2 min, and d) subsequently applying a potential of 0.10 V during 2 min.

Figure 2. Calibration graphs representing the time variation of the $i(A_*(2))/i(A_{Au}(1))$ ratio using samples of known ages in Table 1. Experimental data for samples whose age was known within a range of ±20 years (grey) and samples whose age was know with relatively large uncertainty (pale yellow), see Table 1. Continuous line: curve obtained upon fitting data points to equation in the main text. Insets: photographic images of upper: a *Florín* (Alfonso V, Valencia, 1416-1418 CE), and lower: a *Solidus* (Honorio, Mediolanum, 394-395 CE) whose positions in the diagram are marked by arrows.
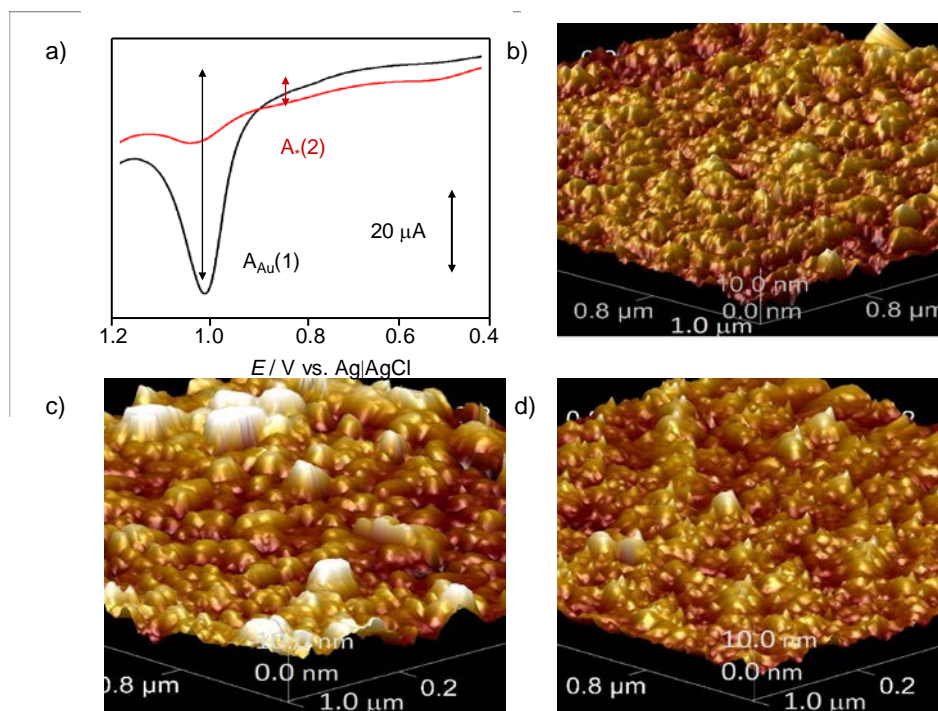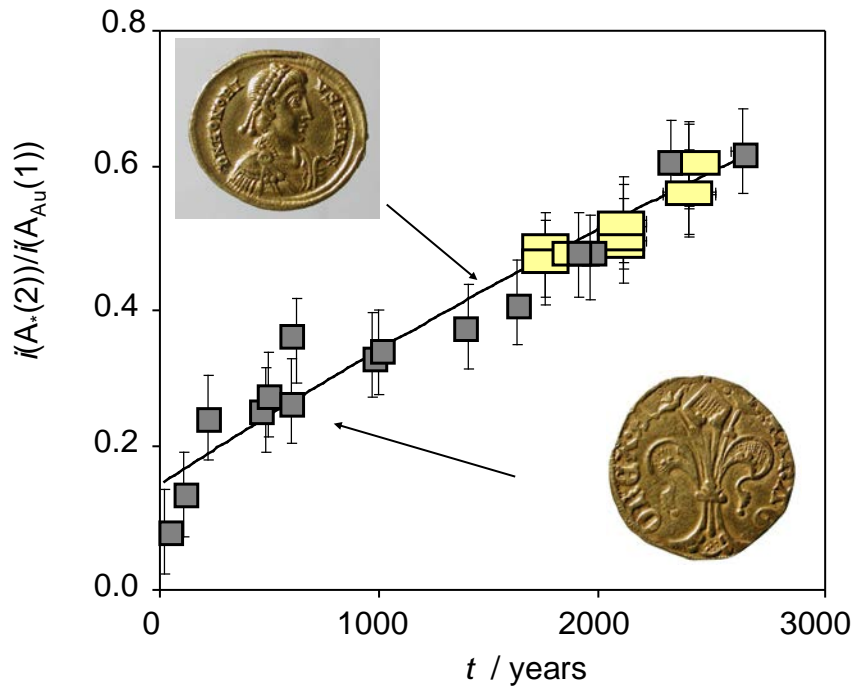
Figure 1.

Figure 2.

Supplementary materials:

Experimental details

Voltammetric experiments were performed via sampling by means of commercial graphite bars (pencil leads; Faber-Castell, HS). These were pressed on plain surfaces of the archaeological objects as described in VIMP literature. Voltammograms (LSVs) were recorded at bare and sample-modified graphite electrodes in contact with air-saturated 0.10 M HCl using CH I660 potentiostat. Blank experiments were carried out with a gold electrode (BAS MF 2012, geometrical area 0.018 cm^2). Electrochemical impedance measurements were performed in the 0.01 to 100000 Hz frequency range with an ac sinusoidal perturbation amplitude of 10 mV (peak-to-peak) at the open circuit potential previously determined.

Raman spectra were obtained by means of a XPlora Horiba MTB model using a 532 nm laser for excitation and keeping the samples in backscattering geometry at room temperature. A 100 confocal microscope objective was used to focus the excitation laser on the sample and to collect the scattered light to the spectrometer with exposure times between 5 and 20 s, 10-50 acquisitions, and laser power varying between 30–90 mW, respectively. Data acquisition was carried out with the LabSpec 6 Spectroscopy Suite from Horiba MTB. For Raman depth measurements, samples were mounted on an *x,y* motorized stage, with *z*-displacement controlled with a piezo-transducer on the objective. The confocal pinhole diameter was 200 mm, and the slit width was 100 mm.

FESEM/EDX analysis was performed with Hitachi S-4800 field emission scanning electron microscope (Tokyo, Japan) operating at 20 kV, and in situ AFM-monitored electrochemical experiments with a multimode AFM (Digital Instruments VEECO Methodology Group, USA) and a NanoScope IIIa controller and equipped with a J-type scanner (max. scan size of 150×150×6 μm). The topography of the samples was studied in peak-force tapping mode. A silicon tip on nitride lever probe Bruker Scanasyst fluid+ (k 0,7 N/m) has been used.

References

F. Scholz, B. Meyer, *Electroanalytical Chemistry, A Series of Advances* **20**, 1 (1998).

F. Scholz, U. Schröder, R. Gulabowski, A. Doménech-Carbó, *Electrochemistry of Immobilized Particles and Droplets*, 2nd ed. Springer, Berlin-Heidelberg, 2005.

A. Doménech-Carbó, J. Labuda, F. Scholz, *Pure Appl. Chem.* **85**, 609 (2013) (IUPAC Technical Report).

A. Doménech-Carbó, M.T. Doménech-Carbó, V. Costa, *Electrochemical Methods in Archaeometry, Conservation and Restoration* (Monographs in Electrochemistry series, F. Scholz, Ed.). Springer, Berlin-Heidelberg, 2009.

Table S.1. Samples of archaeological gold used for calibration purposes. MPV: Museum of Prehistory of Valencia; MB: Museum of Borriana; MC: Museum of Castelló; PV: private collections. Percentages of gold and silver were estimated from the area of the respective voltammetric peaks.

Catalog	Type of object and provenance	Date	Composit. Au/Ag/Cu (%wt)
MPV28926	Hekte, Jonia [MPV]	650-600 BCE	87.8/8.0/4.2
MPV25933	Stater, Cartago[MPV]	310-290 BCE	89.5/8.5/2.0
s/n	Pendant, Orley[MB]	4th BCE	91.3/6.0/2.7
MC1675	Pendant, Puig de la Nau, Benicarló[MC]	400-375 BCE	92.3/4.8/2.9
MC1676	Pendant, Puig de la Nau, Benicarló[MC]	400-375 BCE	91.0/7.0/2.0
MC1678	Pendant, Puig de la Nau, Benicarló[MC]	400-375 BCE	91.0/5.9/2.1
MC0224	Plate, Borriol, Tossalet de les Forques[MC]	100 BCE	92.6/6.2/1.2
MC430	Ring, La Punta, La Vall d'Uixó[MC]	100 BCE	91.6/6.5/2.9
MC2213	Pendant, La Morranda del Ballestar[MC]	100 BCE	91.0/6.0/3.0
MC2233	Pendant, La Morranda del Ballestar[MC]	100 BCE	89.8/8.0/2.2
MC1082	Ring, El Pilonet de Santa Bàrbara de Vilavella, Imperial Roman age[MC]	100 CE	89.0/7.4/2.6
MPV28968	Aureus, Nero, Rome[MPV]	64-65 CE	91.5/6.0/2.5
MC2373a	Needle, Hostalots de Villanueva de Alcolea, Roman age[MC]	3th-4th CE	90.2/7.0/2.8
MC2373a	Needle, Hostalots de Villanueva de Alcolea, Roman age[MC]	3th-4th CE	90.6/7.2/2.2
MPV31042	Solidus, Honorio, Mediolanum[MPV]	394-395 CE	90.0/7.1/2.9
MPV27657	Sisebuto, Tremis, Toledo[MPV]	612-621 CE	88.5/7.4/4.6
s/n	Dinar, Santa Elena hoard[MPV]	1018 CE	89.6/8.1/2.3
s/n	Dinar, Santa Elena hoard[MPV]	11th CE	89.8/8.2/2.2
MPV26660	Ducado, Antonio Venier, Rep. Venezia[MPV]	1382-1400 CE	91.0/5.5/3.5
MPV25914	Florín, Alfonso V, Valencia[MPV]	1416-1418 CE	91.1/6.0/2.9
MPV28941	Escudo, Francisco I, Rouen[MPV]	1519 CE	91.3/5.1/3.6
s/n	Plate, Torre del Rey, Oropesa[MC]	1531 CE	89.0/7.8/4.2
MPV22136	8 escudos, Carolus IV, Nuevo Reino[MPV]	1794 CE	88.6/7.4/4.0
s/n	Medal[PC]	1903 CE	94.1/4.0/1.9
s/n	Ring[PC]	1988 CE	91.6/5.4/3.0

Gold electrochemistry

Figure S.1a shows the cyclic voltammetric response of a gold electrode in 0.10 M H_2SO_4 air-saturated aqueous electrolyte. In the initial anodic scan, an oxidation wave appears at ca. +1.2 V vs. Ag/AgCl (A_{Au}) preceding the rising current above +1.5 V corresponding to the oxygen evolution reaction (OER). In the subsequent cathodic scan, a tall reduction signal appears at ca. +0.90 V (C_{Au}) which is followed by a cathodic wave at −0.10 V, caused by the reduction of dissolved oxygen (oxygen reduction reaction, ORR) which precedes the hydrogen evolution reaction (HER). The voltammetric response in 0.10 M HCl was similar but the signal A_{Au} was significantly enhanced relative to the peak C_{Au} (see Figure S.1b).

The A_{Au} process recorded in H_2SO_4 can be attributed to the initial adsorption of $\cdot$OH to the gold surface, rapidly followed by further oxidation including place exchanges between gold and oxygen atoms, leading to a quasi three-dimensional oxihydrate layer. In turn, the peak C_{Au} corresponds to the reduction of the gold oxide monolayer to gold metal which occurs at potentials clearly separated from A_{Au} because of the significant surface reorganization involved in these processes.

In contact with HCl, however, the oxihydrate formation competes with the chloride-assisted oxidative dissolution of gold to form different Au(III)-chloride complexes. Interestingly, in both HCl and H_2SO_4 electrolytes, the main gold oxidation signal, A_{Au}, is preceded by weak anodic signals (A_*, marked by arrows in Figure 1a) between +0.6 and +1.0 V which are enhanced when the potential scan was started at values more negative than −0.2 V. These signals are attributed to the oxidation of active gold sites, i.e., gold atoms coordinatively unsaturated or occupying defect lattice sites:

$$Au * \xrightarrow{-3e^-} Au^{3+} \xrightarrow{+(n+3)H_2O} Au^{3+} \cdot (n+3)H_2O$$

$$\xrightarrow{-3H^+} Au(OH)_3 \cdot nH_2O \qquad (S.1)$$
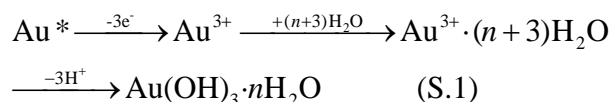
The formation of such active sites has been described as a result of a place-exchange process in which oxygen surface atoms penetrate deeper layers, a situation ultimately related to the spillover features schematized in Figure S.2.

Our voltammetric data indicated a growth of the A_* signals relative to A_{Au} with age, thus suggesting an aging scenario involving adsorption of oxygen species, sub-surface incorporation of oxygen atoms, and formation of coordinatively unsaturated Au sites, which are able to act as electrochemically active centers. This picture was found to be consistent with AFM examination of the gold surfaces during the application of successive oxidative and reductive potential inputs illustrated in Figures 1b-d, corresponding to topographic images of a microcrystalline gold plate in contact with 0.10 M H_2SO_4 aqueous solution. After applying an oxidative input at the potential of A_{Au}, the gold surface, which originally exhibited a relatively uniform roughness (Fig. 1b), became slightly rougher and covered by rounded features alternated with several gross features (Fig. 1c) attributable to local formations of gross oxide humps. The subsequent application of a reductive potential to this oxidized surface regenerates a gold surface whose roughness differs from the parent surface, also incorporating peaked features and retaining few gross humps (Fig. 1d).

References

U. Hasse, H. Wulff, C.A. Helm, F. Scholz, *J. Solid State Electrochem*. **17**, 3047 (2013).

R.L. Doyle, M.E.G. Lyons, *J. Solid State Electrochem*. **18**, 3271 (2014).

L.D. Burke, A.P. O'Mullane, *J. Solid State Electrochem*. **2000**, *4*, 285 (2000).

S. Cherevko, N. Kulyk, C.-H. Chung, *Electrochim. Acta* 69, 190 (2012).

J. Herrera-Gallego, C.E. Castellano, A. Calandra, A.J. Arvia, *J. Electroanal. Chem*. **66**, 207 (1975).

S. Cherevko, N. Kulyk, C.-H. Chung, *Electrochim. Acta* **69**, 190 (2012).

C. Jeyabharathi, U. Hasse, P. Ahrens, F. Scholz, *J. Solid State Electrochem*. **18**, 3299 (2014).

C. Jeyabharathi, U. Hasse, P. Ahrens, F. Scholz, *J. Solid State Electrochem*. **20**, 3025 (2016).

U. Hasse, H. Wulff, C.A. Helm, F. Scholz, Grain boundary corrosion of the surface of annealed thin layers of gold by OH·radicals. *J. Solid State Electrochem*. **16**, 2383 (2012).

U. Hasse, H. Wulff, C.A. Helm, F. Scholz, *J. Solid State Electrochem*. **17**, 3047 (2013).

H. Angerstein-Kozlowska, B.E. Conway, A. Hamelin, L. Stoicoviciu, *Electrochim. Acta* **31**, 1051 (1986).

H. Angerstein-Kozlowska, B.E. Conway, A. Hamelin, L. Stoicoviciu,. *J. Electroanal. Chem*. **228**, 429 (1987).

Figure S.1. Cyclic voltammograms of a polycrystalline gold electrode in contact with: a) 0.10 M H_2SO_4, and b) 0.10 M HCl air-saturated aqueous solutions. Potential scan rate 50 mV s^{-1}.
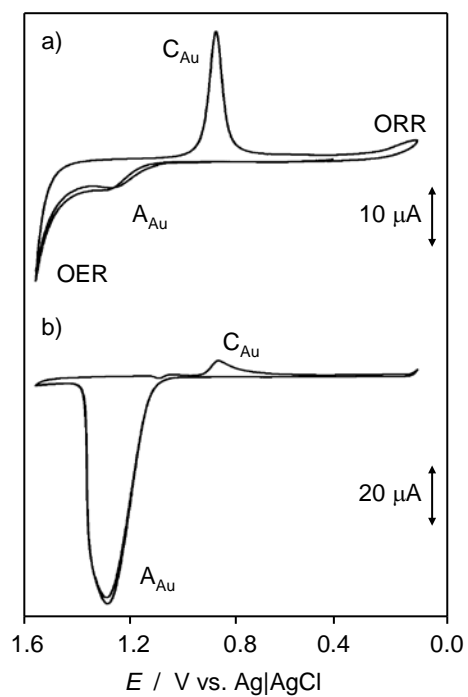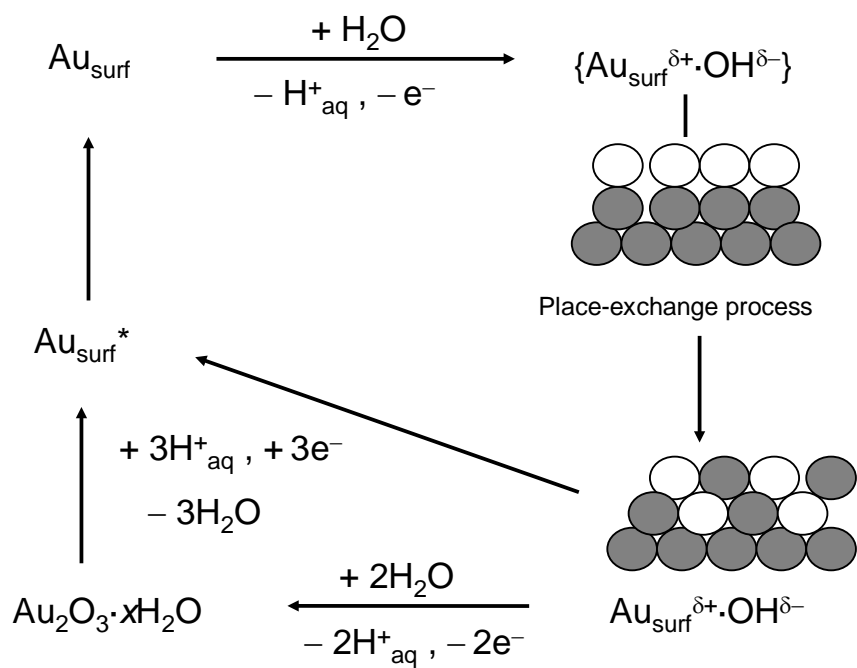
Figure S.2. Scheme of the formation of active gold sites during electrochemical turnovers applied to gold surfaces.

Au_{surf} $\xrightarrow[- H^+_{aq} ,\; - e^-]{+ H_2O}$ $\{Au_{surf}^{\delta+}\cdot OH^{\delta-}\}$

Place-exchange process

Au_{surf}^*

$+ 3H^+_{aq} ,\; + 3e^-$

$- 3H_2O$

$Au_2O_3\cdot xH_2O$ $\xleftarrow[- 2H^+_{aq} ,\; - 2e^-]{+ 2H_2O}$ $Au_{surf}^{\delta+}\cdot OH^{\delta-}$

Voltammetry of archaeological gold

Our voltammetric data indicated a growth of the A_* signals relative to A_{Au} with age, thus suggesting an aging scenario involving adsorption of oxygen species, sub-surface incorporation of oxygen atoms, and formation of coordinatively unsaturated Au sites, which are able to act as electrochemically active centers. This picture was found to be consistent with AFM examination of the gold surfaces during the application of successive oxidative and reductive potential inputs illustrated in Figures 1b-d, corresponding to topographic images of a microcrystalline gold plate in contact with 0.10 M H_2SO_4 aqueous solution. After applying an oxidative input at the potential of A_{Au}, the gold surface, which originally exhibited a relatively uniform roughness (Fig. 1b), became slightly rougher and covered by rounded features alternated with several gross features (Fig. 1c) attributable to local formations of gross oxide humps. The subsequent application of a reductive potential to this oxidized surface regenerates a gold surface whose roughness differs from the parent surface, also incorporating peaked features and retaining few gross humps (Fig. 1d). These observations are consistent with an increase of coordinatively unsaturated gold sites with age, also in agreement with studies on the attack of gold surfaces by $\cdot$OH radicals. [19]

In order to study archaeological samples, the sequence of linear potential scan voltammograms (LSVs) depicted in Figures S.3 and S.4 was applied to gold nanosamples extracted from gold objects by means of graphite pencils (see Supplementary information). In the initial anodic scan (Fig. S.3a), a main anodic peak appears at ca. +1.05 V vs. Ag/AgCl ($A_{Au}(1)$) which is preceded by a weak shoulder at ca. +0.85 V ($A_*(1)$) and followed by a shoulder near to +1.2 V and a subsequent prominent rising current. This last corresponds to the OER process. In the subsequent cathodic scan (Fig. S.3b), a cathodic peak at +0.45 V ($C_{Au}(1)$) was recorded, frequently accompanied by a second signal at ca. −0.05 V (C_{Ag}) corresponding to the reduction of AgCl. In the second anodic scan (Fig. S.3c), this signal is accompanied by its corresponding anodic stripping peak (A_{Ag}) and followed by oxidation waves at +0.85 V ($A_*(2)$) and +1.05 V ($A_{Au}(2)$). Remarkably, the main gold-localized oxidation signal A_{Au} is diminished in the second scan relative to the first one while the signal A_* is enhanced (see Fig. S.3d).

Figure S.3. LSVs of a sample of a gold ring attached to graphite electrode in contact with 0.10 HCl aqueous solution. Black lines: sample-modified electrode; red lines: unmodified graphite electrode submitted to the same sequence of potential scans. a) initial anodic scan; b) subsequent cathodic scan; c) 2nd anodic scan. d) Detail of the anodic region superimposing the 1st (black) and 2nd (red) anodic scans. Potential scan rate 50 mV s^{-1}.
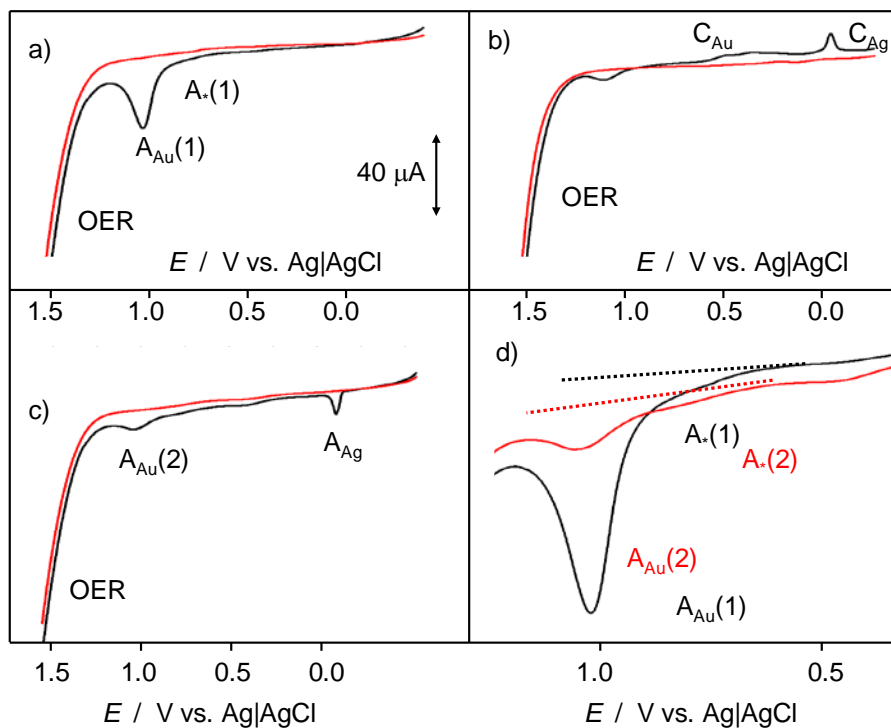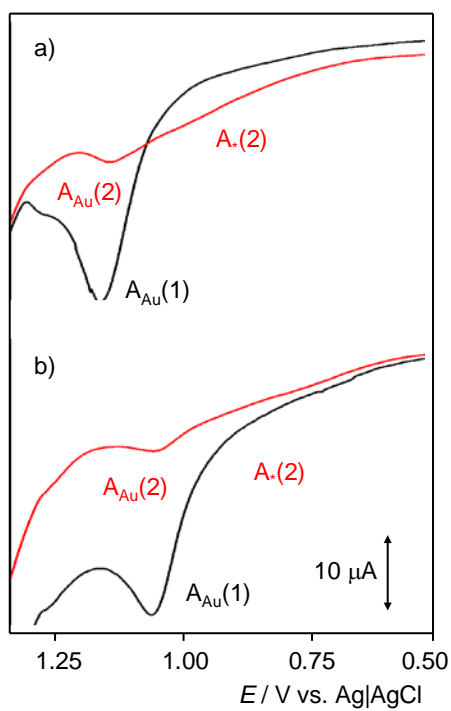
Figure S.4. LSVs of nanosamples from a) Santa Elena *dinar* emitted in 1018 and b) a Carolus IV *escudo* minted in Spain in 1794 attached to a graphite electrodes in contact with 0.10 M HCl (black lines) and at unmodified graphite electrodes (red lines). Potential scan initiated at -0.05 V vs. Ag/AgCl in the positive direction; potential scan rate 50 mV s^{-1}.

Under the used conditions, pressing the graphite bars (vide infra) onto the gold surface ensures transfer of gold at the nanogram level, as estimated from SEM/EDX observation of graphite bars after sampling (Figure S.5). Sampling yields a few gold plates 0.1 – 0.5 μm sized adhering to the graphite laminas, which, after applying an oxidative potential in 0.10 M HCl become narrowed, consistently with the occurrence of a smooth oxidative dissolution (Supplementary information, Figure S.6).

Figure S.5. SEM images of a graphite plate a) before and b) after sampling on gold ring from 1988. c) EDX spectrum of the region covered in b) showing Au lines accompanied by weak Cu and Si associated to clay residuals of graphite polishing (see Experimental details).
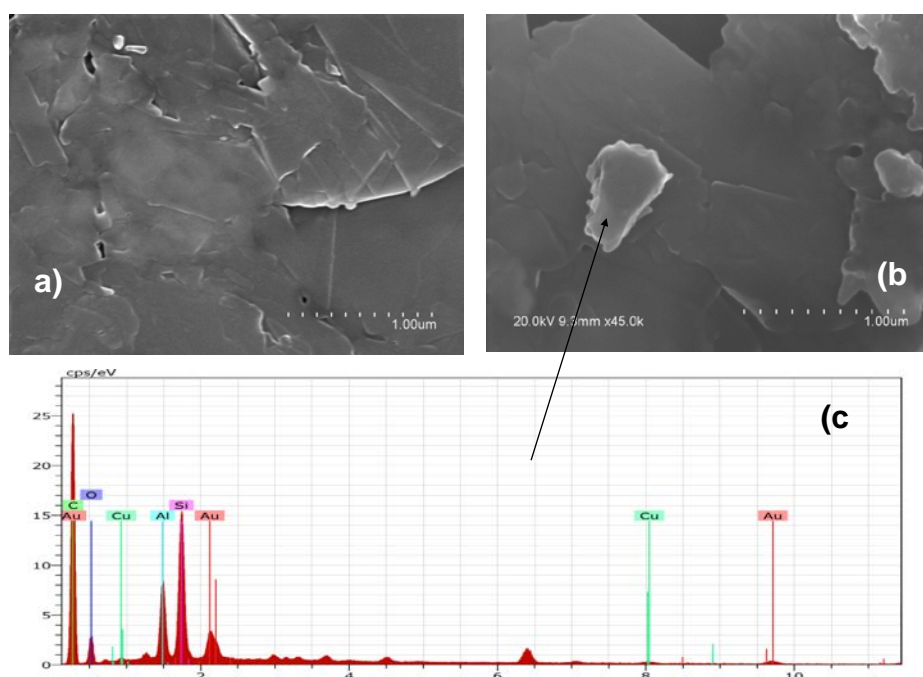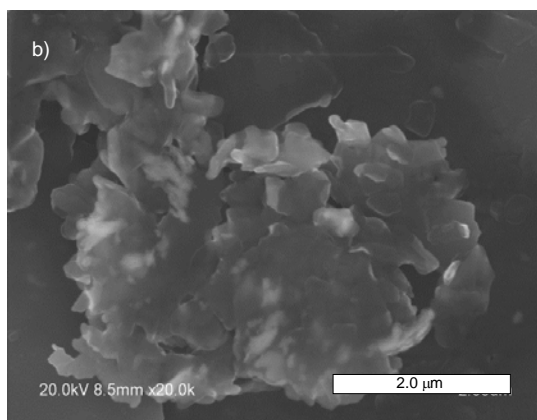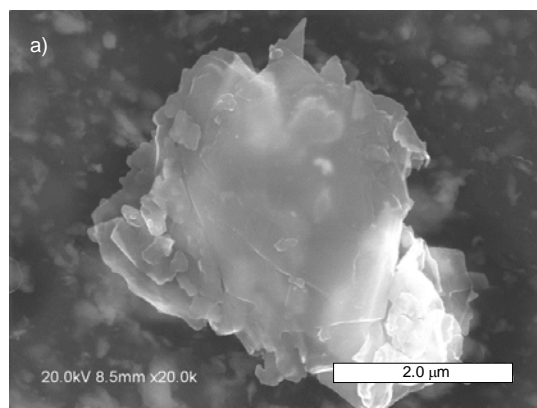
Figure S.6. Secondary electron images of gold plates from a medal fabricated in 1903 abrasively transferred onto a graphite bar in contact with 0.10 M HCl aqueous solution: a) before and b) after application of a potential step of +1.25 V for 5 min.

Examination of gold surfaces using Raman spectroscopy indicated the presence of different oxygen species displaying different concentration gradients in the gold surface layer, namely, adsorbed $\cdot$O on Au(111) and Au(211) faces (bands at 361 cm^{-1} and 449 cm^{-1}), $\cdot$OH and $\cdot$OOH (O-O stretching at 800 cm^{-1}), and O_2.(1000 cm^{-1}) and Au(OH)$_3$ and Au$_2$O$_3$ species (bands at 650 and 635 cm^{-1}). Our Raman measurements on gold performed at different depths using a x,y,z-motorized stage, revealed the presence of the above bands, those corresponding to adsorbed species decreasing with depth contrarily to gold oxide and oxo-hydroxide bands, see Figures S.7, S.8.

References

O. Diaz-Morales, F. Calle-Vallejo, C. de Munck, M.T.M. Koper, *Chem. Sci*. **4**, 2334 (2013).

J. Desilvestro, M.J. Weaver, *J. Electroanal. Chem*. **209**, 377 (1986).

B.S. Yeo, S.L. Klaus, P.N. Ross, R.A. Mathies, A.T. Bell, *ChemPhysChem* **11** 1854 (2010)

N. Montoya, E. Montagna, Y. Lee, M.T. Doménech-Carbó, A. Doménech-Carbó, *J. Raman Spectrosc*. **48**, 1337 (2017).

Figure S.7. Raman spectra at two different depths of a gold medal dated to 1903. Exposure time 15 s, 40 acquisitions and laser power 60 mW.
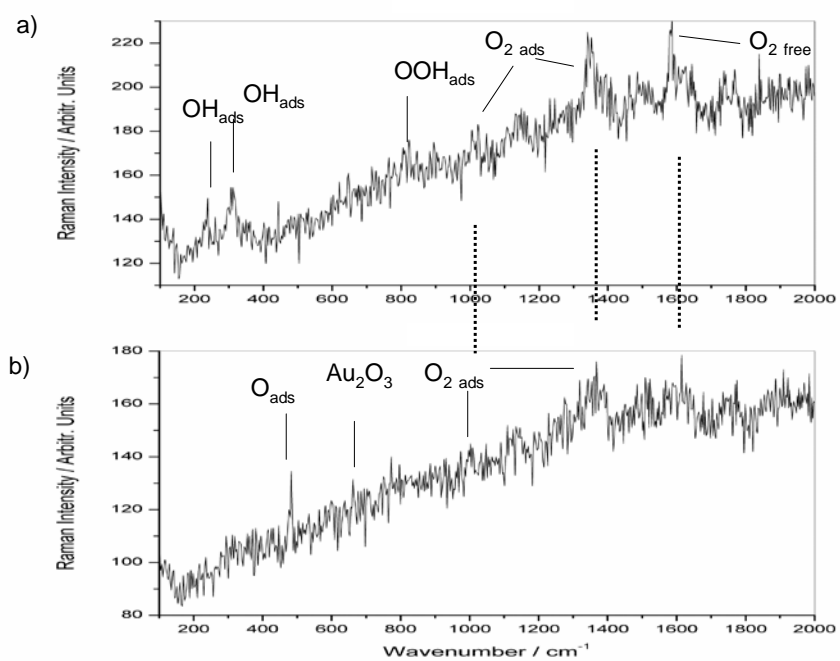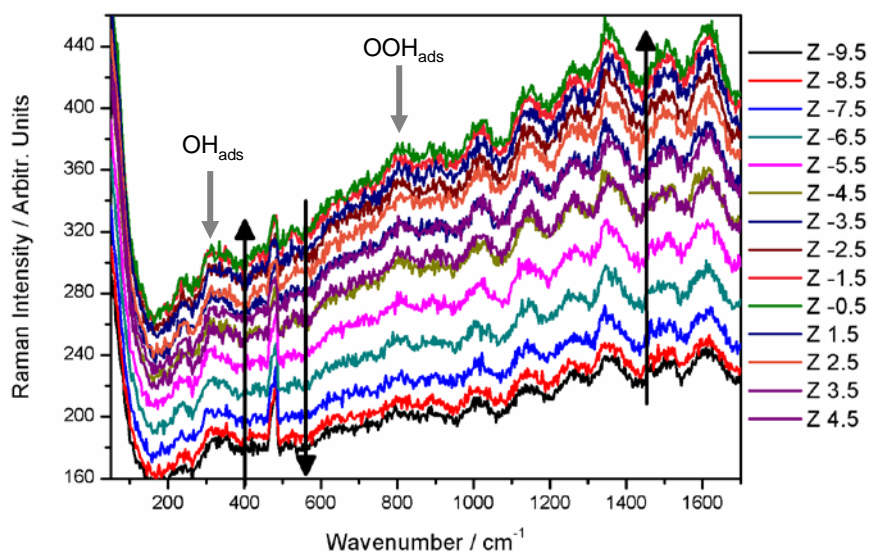
Figure S.8. Raman spectra of a gold medal from 1903 at different depths. The bands characterizing adsorbed OH and OOH are marked by arrows.

Voltammetric dating

The voltammetric features in Figures 1a, S.3 and S.4 can be interpreted assuming that the oxidative dissolution dominates the oxidation pathway of gold in HCl. Accordingly, the 1st anodic scan will form a 'clean' gold surface retaining defect sites associated to aging, then recording the $A_{Au}(1)$ and $A_*(1)$ signals. In the subsequent cathodic scan, (process C_{Au}) a deposit of gold is formed on the previous surface thus maintaining or increasing the number of defect sites. As a result, a second anodic scan produces an enhanced signal for the oxidation of active gold sites, $A_*(2)$; i.e., the applied potential turnovers amplify the signal for active/defect gold sites (see a schematic representation in Figure S.9 of Supplementary materials).

Figure S.10 depicts the variation of $i(A_*(2))/i(A_{Au}(1))$ vs. $i(A_{Au}(1))$ for several sample-modified graphite electrodes in contact with 0.10 HCl taken from peak current measurements in the sequence of voltammograms such as in Figures 1a, S.3 and S.4. This figure compares the graphs determined for replicate measurements on nanosamples from a Cartago coin (310-290 BCE), a Visigothic coin (612-621 CE) and a medal and a ring produced in 1903 and 1988, respectively. Clearly, the $i(A_*(2))/i(A_{Au}(1))$ varies with the value of $i(A_{Au}(1))$, a feature which can be rationalized on assuming that sampling with graphite pencil on the metal surface removes more or less deep gold and oxygen species and active sites have a depth dependent distribution. Since gold aging implies a relative increase of active sites, the depth distribution of the same will be also age-dependent. Experimental data were consistent with the application of a potential law for describing the in depth distribution of oxygen species and gold active sites, as described in the Annex A.1 of the Supplementary information. The following potential law, similar to that tested for copper/bronze corrosion products can be expressed as:

$$\frac{i(A_*(2))}{i(A_{Au}(1))} \approx B + Di(A_{Au}(1))^\delta \qquad (S.2)$$

where B and D are constants depending on the electrochemical conditions and the density of oxygen species and active gold sites on the external gold surface. Since these last parameters vary with age, the coefficients B and D will be age-dependent. Accordingly, as can be seen in Figure S.10, the $i(A_*(2))/i(A_{Au}(1))$ vs. $i(A_{Au}(1))$ curves will vary with age. The consistency of the model was tested using the variation of $i(C_{Au}(1))$ on $i(A_{Au}(1))$, the predicted linear variation being satisfied by experimental data (see Supplementary information, Annex A.1 and Figure S.11).

Since the $i(A_*(2))/i(A_{Au}(1))$ vs. $i(A_{Au}(1))$ curves in Figure S.10 can be viewed as isochronous graphs each one representing the voltammetric response of aged gold at a given time, they can be used for dating purposes after the corresponding calibration with a set of samples of known age.

In order to construct a calibration graph for dating, a practical problem was the increase in the uncertainty in the values of the $i(A_*(2))/i(A_{Au}(1))$ ratio at low $i(A_{Au}(1))$ values, thus resulting in an increase in the uncertainty associated to the parameter B calculated from curve fitting. To avoid this problem, the calibration data were taken as those interpolated in curves such as in Figure S.10 to a current $i(A_{Au}(1))$ of 60 µA. Figure 2 in the main text presents the calibration data expressed as the time variation of the

$i(A_*(2))/i(A_{Au}(1))$ ratio (determined as the value interpolated at $i(A_{Au}(1)) = 60$ µA in $i(A_*(2))/i(A_{Au}(1))$ vs. $i(A_{Au}(1))$ graphs such as in Figure S.10) using samples whose age was known within a range of ±20 years in Table S,1. After testing different models for adsorption kinetics, the more satisfactory fit was obtained for Lagergren's equation (16), corresponding to a pseudo-first order rate law, rewritten here as:

$$\frac{i(A_*(2))}{i(A_{Au}(1))} = H - Qe^{-kt} \qquad (S.3)$$

Analysis of errors is presented as an Annex (Annex A.2) accompanied by Figure S.12.

References

A. Doménech-Carbó, M.T. Doménech-Carbó, E. Montagna, Y. Lee, Talanta **169**, 50 (2017).

F. Di Turo, N. Montoya, J. Piquero-Cilla, C. De Vito, F. Coletti, G. Favero, A. Doménech-Carbó, *Anal. Chim. Acta* **955**, 36 (2017).

W. Plazinski, W. Rudzinski, *J. Phys. Chem. C* **113**, 12495 (2009).

Figure S.9. Scheme of the aging of gold surfaces and the subsequent application of electrochemical turnovers following the sequence of anodic/cathodic/anodic successive potential scans illustrated in Figure 2. White arrow marks defect sites generated by aging and blue arrows mark defect sites generated electrochemically.
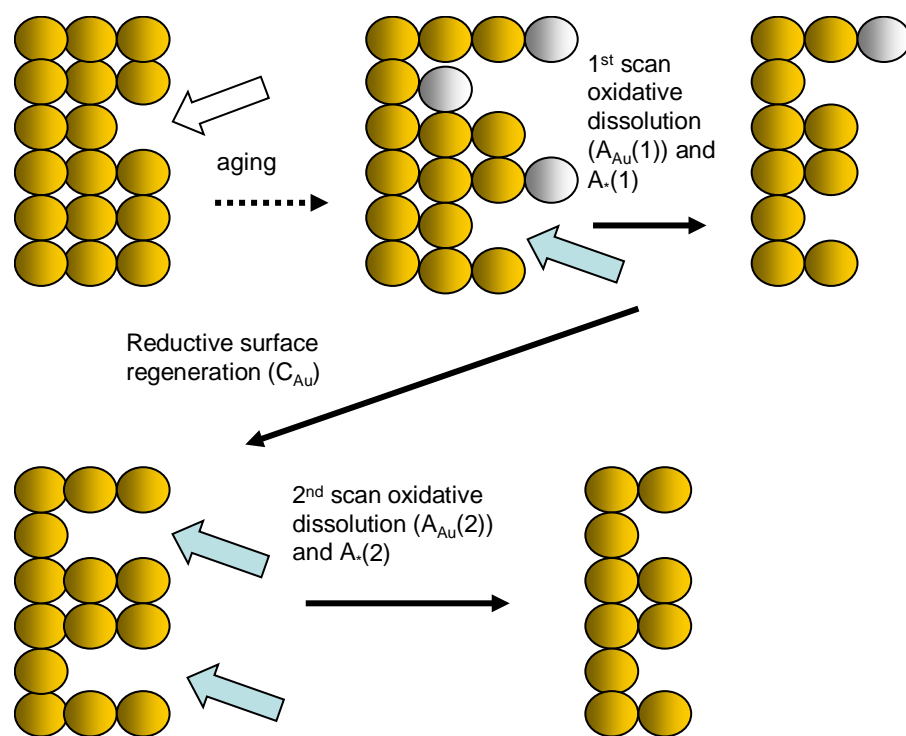
Figure S.10. Plots of $i(A_*(2))/i(A_{Au}(1))$ vs. $i(A_{Au}(1))$ for sample-modified graphite electrodes in contact with 0.10 HCl. Data from the sequence of voltammograms such as in Figure 3. Inset: photographic image of sample MC1675, Iberian-Roman pendant from Puig de la Nau, Benicarló, Spain, 400-375 BCE.
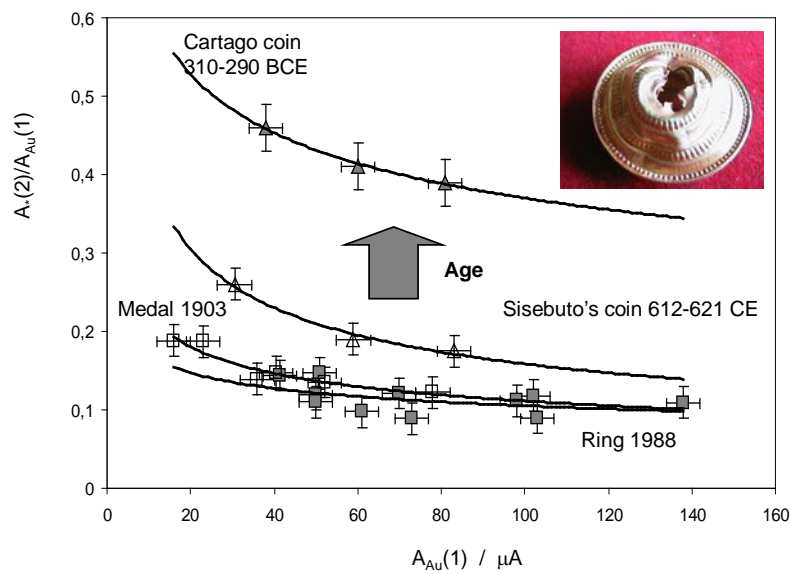
Figure S.11. Variation of $i(C_{Au}(1))$ on $i(A_{Au}(1))$ in successive LSVs at sample-modified graphite electrodes immersed into 0.10 M HCl for ring fabricated in 1988 (squares), medal from 1903 (solid squares) and a *florin* coin, corresponding to the reign of *Alfonso* V, minted in 1416-1418. Experimental conditions such as described in Figure 2. In agreement with the predictions from Eqs. (3) and (4), the plots can be fitted to straight lines passing by the origin.
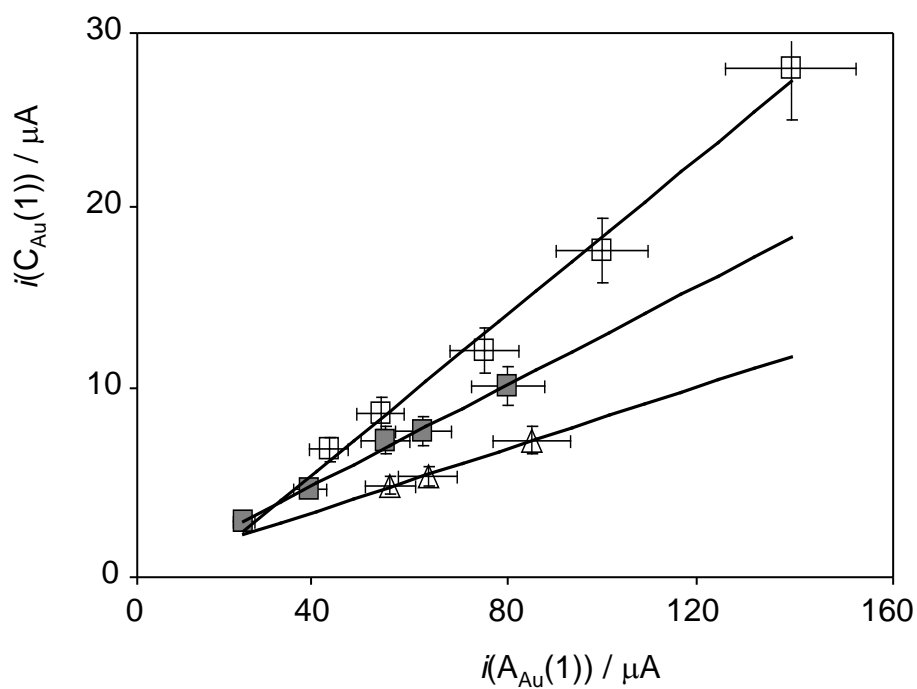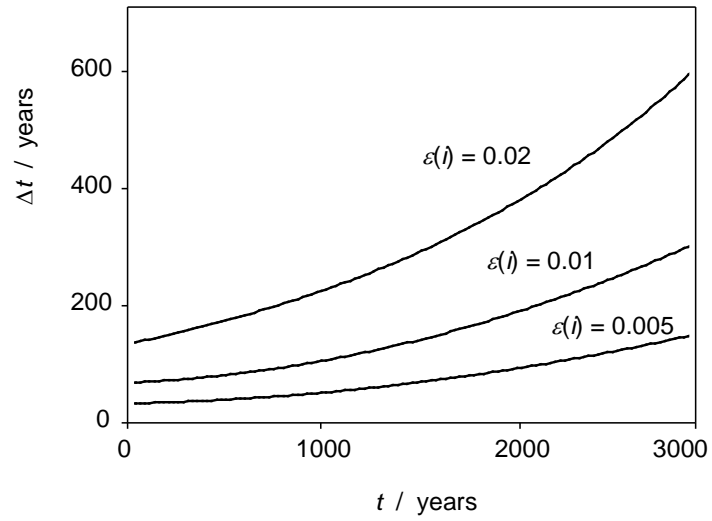
Figure S.12. Theoretical variation of the absolute uncertainty in age estimates from Eq. (A.2.6) using the calibration equation (Eq. (3)) for gold dating taking $H = 0.71\pm0.05$, $Q = 0.58\pm0.08$, and $k = (5.8\pm0.4) \times 10^{-4}$ years^{-1}, for three values of $\varepsilon(i)$.

Annex I: Modeling voltammetric measurements

Measurements of peak currents/peak areas of the discussed processes were consistent with the foregoing set of hypotheses taking a simplified model of gold aging. This is based on the assumption that oxygen species are distributed in a narrow region of thickness x_o of the gold surface so that that the number of adsorbed oxygenated species per volume unit, n_{ox} decreases with the depth x in the external region of the gold surface following a potential law of the type $n_{ox} = g_{ox} n_{ox}^{sup} z^\delta$, where z is a non-dimensional depth defined as $z = 1 - x/x_o$, and n_{ox}^{sup} represents the surface number of oxygenated species per volume unit and g_{ox} a constant. On first examination, one can assume that the number of electrochemically accessible gold centers, n_{Au}, varies inversely, i.e.: $n_{Au} = n_{Au}^o - g_{ox} n_{ox}^{sup} z^\delta$, n_{Au}^o being the average density of Au atoms in the metal bulk.

In voltammetric experiments under fixed conditions, the peak current (and/or peak area, equivalent under our experimental conditions, see Figure S.3 of Supplementary materials) measured for the voltammetric peaks $A_{Au}(1)$, $i(A_{Au}(1))$, should be proportional to the total number of gold atoms extracted from the corrosion layers during the sampling process. Ideally, in the sampling process, a lamina of gold surface area S was extracted and transferred onto the electrode surface so that, one can write:

$$i(A_{Au}(1)) = \int_0^z k_{A1}(n_{Au}^o - g_{ox} n_{ox}^{sup} z^\delta) S dz \quad (A.1.1)$$

Here, k_{A1} is an electrochemical constant depending on the electrolyte, potential scan rate and graphite type. This signal is preceded by the $A_*(1)$ wave representative of the oxidation of active sites. The corresponding peak current/peak area will be:

$$i(A_*(1)) = \int_0^z k_{A1}(n_{Au}^o - g_* n_*^{sup} z^\lambda) S dz \quad (A.1.2)$$

As a result, after the first anodic scan, there is a certain depth distribution of oxidized gold forms and active sites. Then, the density of oxidized gold at a depth z will be:

$$n_{ox} = g_{ox} n_{ox}^{sup} z^\delta + h_{Au}(n_{Au}^o - g_{ox} n_{ox}^{sup} z^\delta) \quad (A.1.3)$$,

where h_{Au} represents the fraction of Au atoms effectively oxidized in the process $A_{Au}(1)$. Similarly,

$$n_* = g_* n_*^{sup} z^\lambda + h_*(n_{Au}^o - g_* n_*^{sup} z^\lambda) \quad (A.1.4)$$

and, neglecting the contribution of oxidized gold active sites, and taking h_{Au} as a constant, the peak current/peak area for the process $C_{Au}(1)$ will be:

$$i(C_{Au}(1)) = \int_0^z k_{C1}[h_{Au} n_{Au}^o + (1 - h_{Au}) g_{ox} n_{ox}^{sup} z^\delta) S dz \quad (A.1.5)$$

Then, the $i(C_{Au}(1))/i(A_{Au}(1))$ ratio will be:

$$\frac{i(C_{Au}(1))}{i(A_{Au}(1))} = \frac{k_{C1}S\left(h_{Au}n^{o}_{Au}z + \dfrac{(1-h_{Au})g_{ox}n^{sup}_{ox}z^{1+\delta}}{1+\delta} \right)}{k_{A1}S\left(n^{o}_{Au}z - \dfrac{g_{ox}n^{sup}_{ox}z^{1+\delta}}{1+\delta} \right)} \qquad (A.1.6)$$

Since, even in considerably aged gold surfaces, the density of oxygen species has to be low, one can expect that $n^{o}_{Au}z \gg g_{ox}n^{sup}_{ox}z^{\delta}$, so that the $i(C_{Au}(1))/i(A_{Au}(1))$ ratio will be approximately constant and equal to $h_{Au}(k_{C1}/k_{A1})$. This prediction is in agreement with experimental data (see Supplementary materials, Figure S.4).

As previously noted, following the aforementioned sequence of voltammograms (Figure 5), the process $C_{Au}(1)$ must generate more active gold sites thus resulting, when a second anodic scan is subsequently carried out, in an increase of the intensity of the process A_* in the second scan, $i(A_*(2))$, whereas the remaining original gold produces an oxidation signal of intensity $i(A_{Au}(2))$ diminished relative to its 1st scan wave. Then, the resulting distribution of gold active sites will be:

$$n_* = g_*n^{sup}_*z^{\lambda} + h_*(n^{o}_{Au} - g_*n^{sup}_*z^{\delta}) + h_{**}[g_{ox}n^{sup}_{ox}z^{\delta} + h_{Au}(n^{o}_{Au} - g_{ox}n^{sup}_{ox}z^{\delta})] \qquad (A.1.7)$$

where h_{**} denotes the fraction of oxidized gold converted into new gold active sites during the process $C_{Au}(1)$. Similarly, the fraction of gold remaining in its original form (i.e., previous to the electrochemical turnovers) will be:

$$n_{ox} = n^{o}_{Au} - [g_{ox}n^{sup}_{ox}z^{\delta} + h_{Au}(n^{o}_{Au} - g_{ox}n^{sup}_{ox}z^{\delta})] \qquad (A.1.8)$$

Accordingly, the peak currents/peak areas of the above processes, $i(A_*(2))$ and $i(A_{Au}(2))$ can be expressed as:

$$i(A_{Au}(2)) = \int_{0}^{z} k_{A1}[n^{o}_{Au} - g_{ox}n^{sup}_{ox}z^{\delta}](1-h_{Au})Sdz \quad (A.1.9)$$

$$i(A_*(2)) = \int_{0}^{z} k_{A2}[(h_* + h_{**}h_{Au})n^{o}_{Au} + g_*n^{sup}_*(z^{\lambda} - z^{\delta}) + g_{ox}(h_* + h_{Au})z^{\delta}]Sdz \quad (A.1.10)$$

Integrating and combining the Eqs. (A.1.2) and (A.1.10) one obtains:

$$\frac{i(A_*(2))}{i(A_{Au}(1))} = \frac{k_{A2}S\left[(h_* + h_{**}h_{Au})n^{o}_{Au}z + g_*n^{sup}_*\left(\dfrac{z^{1+\lambda}}{1+\lambda} - \dfrac{z^{1+\delta}}{1+\delta} \right) + g_{ox}(h_* + h_{Au})\dfrac{z^{1+\delta}}{1+\delta} \right]}{k_{A1}S\left(n^{o}_{Au}z - \dfrac{g_{ox}n^{sup}_{ox}z^{1+\delta}}{1+\delta} \right)} \qquad (A.1.11)$$

Assuming that $n_{Au}^o z \gg \dfrac{g_{ox} n_{ox}^o}{1+\delta} z^{1+\delta}$, and that $\lambda \approx \delta$, which, in principle, are reasonable approximations in view of the low level of oxidation of the gold surfaces, one can write:

$$\frac{i(A_*(2))}{i(A_{Au}(1))} \approx \frac{k_{A2}}{k_{A1}}\left[1 + Gz^\delta\right] \qquad (A.1.12)$$

where G is a constant depending on the values of h_{Au}, h_*, h_{**}, g_*, g_{ox}, n_{Au}^o and n_*^{sup}. Then, approximating:

$$i(A_{Au}(1)) \approx k_{A1} S n_{Au}^o z \qquad (A.1.13)$$

one obtains:

$$\frac{i(A_*(2))}{i(A_{Au}(1))} \approx \frac{k_{A2}}{k_{A1}}\left[1 + H i(A_{Au}(1))^\delta\right] \qquad (A.1.14)$$

where H is a constant depending on the values of h_{Au}, h_*, h_{**}, g_*, g_{ox}, n_{Au}^o , n_*^{sup} and S. This equation predicts a variation of $i(A_*(2))/i(A_{Au}(1))$ on $i(A_{Au}(1))$ which is consistent with experimental data showed in Figure 6.

For our purposes, the relevant point to emphasize is that the electrochemical runs produce an effect of amplification of the density of active gold sites and that this effect should increase with the age of the artifact so that one can approximate:

$$age \propto \frac{n_{active\,sites}}{n_{Au}^o} \approx \frac{(h_* + h_{**} h_{Au}) n_{Au}^o}{n_{Au}^o} \approx \frac{k_{A1}}{k_{A2}} \frac{i(A_*(2))}{i(A_{Au}(1))} \qquad (A.1.15)$$

This means that, under the above approximations, the values of the $i(A_*(2))/i(A_{Au}(1))$ ratio can be used for establishing the age of gold samples.

Annex A.2. Analysis of errors in age estimates.

Let us consider a kinetic law of the type:

$$I(t) = H + Qe^{-kt} \qquad (A.2.1)$$

where I denotes a peak current (or peak area) ratio $i(A_*(2))/i(A_{Au}(1))$. Assuming that the values of the constants Q, R and α are well-known, the absolute uncertainties of I and t will be related by the expression:

$$\Delta I(t) = Qke^{-kt}\Delta t \qquad (A.2.2)$$

In turn, the uncertainty in I will be dependent on the uncertainty of the individual measurements of the $i(A_*(2))$ and $i(A_{Au}(1))$ peak currents. Taking $\Delta i = \Delta\, i(A_*(2)) = \Delta\, i(A_{Au}(1)) = $ constant for each series of experiments:

$$\frac{\Delta I(t)}{I(t)} = \frac{\Delta i(A_*(2))}{i(A_*(2))} + \frac{\Delta i(A_{Au}(1))}{i(A_{Au}(1))} \qquad (A.2.3)$$

$$\Delta I(t) = \frac{\Delta i}{i(A_{Au}(1))}\big(1 + I(t)\big) \qquad (A.2.4)$$

Since calibration graphs were obtained from peak current measurements interpolated to a fixed $i(A_{Au}(1))$ value (see main text), the $\Delta i/i(A_{Au}(1))$ can be considered as a constant, $\varepsilon(i)$, so that:

$$\varepsilon(i)[1 + I(t)] = Qke^{-kt}\Delta t \qquad (A.2.5)$$

This means that the uncertainty associated to time estimates will be:

$$\Delta t = \varepsilon(i)\frac{1 + I(t)}{Qke^{-kt}} = \varepsilon(i)\frac{1 + H + Qe^{-kt}}{Qke^{-kt}} \qquad (A.2.6)$$